

In Vivo Magnetic Resonance Imaging for Investigating the Development and Distribution of Experimental Brain Metastases due to Breast Cancer¹

Mevan Perera^{*,2}, Emeline J. Ribot^{*,2},
Dean B. Percy^{*}, Catherine McFadden^{*},
Carmen Simedrea[†], Diane Palmieri[‡],
Ann F. Chambers^{†,§} and Paula J. Foster^{*,§}

^{*}Robarts Research Institute, London, Ontario, Canada;

[†]London Regional Cancer Program, London, Ontario, Canada; [‡]National Cancer Institute, Bethesda, MD;

[§]Department of Medical Biophysics, University of Western Ontario, London, Ontario, Canada

Abstract

INTRODUCTION: The overall goal of this study was to assess the utility of three-dimensional magnetic resonance imaging (MRI) for monitoring the temporal and spatial development of experimental brain metastasis in mice. **MATERIALS AND METHODS:** Brain metastatic human breast cancer cells (231-BR or 231-BR-HER2) were injected intracardially in nude mice for delivery to the brain. Mouse brains were imaged *in vivo* at different time points using a balanced steady-state-free precession (bSSFP) pulse sequence at 1.5 T. Brains were categorized into four regions: cortex, central brain, olfactory, and posterior. The number of metastases and their volumes were quantified for both cell lines. **RESULTS:** There was no difference in the mean number of metastases for either cell line. The volumes of metastases in mice injected with 231-BR-HER2 cells were significantly larger than those for mice injected with 231-BR cells. The growth rate for 231-BR-HER2 metastases was 67.5% compared with 54.4% for the 231-BR metastases. More than 50% of metastases were located in the cortex and 25% to 30% of metastases were identified in the central brain for each time point and for mice injected with either cell line. The volumes of metastases were significantly larger in mice with fewer metastases at end point. **SIGNIFICANT CONCLUSIONS:** MRI provided a comprehensive accounting of the number and size of experimental brain metastases in the whole mouse brain at multiple time points. This approach has provided new information about the temporal and spatial development of metastases in the brain not possible by other histopathologic or imaging methods.

Translational Oncology (2012) 5, 217–225

Introduction

Traditionally, it has been reported that up to 20% of metastatic breast cancer patients will develop brain metastases; however, this number may be as high as 35% in patients with human epidermal growth factor receptor 2 (HER2/neu)-expressing breast cancer [1–5]. Untreated, the median survival time is 2 to 3 months, and even with aggressive treatment, survival is usually extended only marginally, 4 to 12 months [6]. The incidence of brain metastases in breast cancer patients is increasing [7], especially for patients with HER2/neu-expressing breast cancer [8]. This is attributed to patients surviving primary cancers for longer periods because of improved therapeutic agents that successfully treat most systemic but not brain metastases [9,10].

To study breast cancer metastasis to the brain, mouse models have been developed using human breast cancer cell lines [11–15]. Metastases have been characterized mainly by histology, immunohistochemistry, and fluorescence microscopy in these models [16–18].

Address all correspondence to: Dr Paula J. Foster, Imaging Laboratories, Robarts Research Institute, 100 Perth Dr, London, Ontario, Canada N6A 5K8. E-mail: pfoster@imaging.robarts.ca

¹This work was supported by the US Army Medical Research and Materiel Command under W81XWH-06-2-0033.

²Equally contributed as first authors.

Received 4 February 2012; Revised 4 February 2012; Accepted 14 February 2012

Copyright © 2012 Neoplasia Press, Inc. All rights reserved 1944-7124/12/\$25.00
DOI 10.1593/do.12109

These techniques allow for measurements of the numbers of metastases and the cross-sectional area of metastases and for an analysis of cellular markers. Although these methods are able to provide detailed molecular and morphologic information, they are limited by the need to sacrifice the animal, and only an end point analysis is permitted. *In vivo* imaging methods are key to a better understanding of the progression of brain metastases.

A wealth of information can be derived about the development of metastases from *in vivo* three-dimensional magnetic resonance imaging (MRI). MRI is noninvasive and therefore permits multiple scanning sessions to be performed to monitor the temporal features of metastasis, whereas histology only permits a single snapshot in time. MR images can be acquired in three dimensions, allowing the whole brain to be analyzed in all spatial orientations and without gaps between slices; this is unlike histologic analyses where it is a practical impossibility to analyze the whole brain, section by section. Metastases volumes can be measured from three-dimensional MRI, which represent their size *in vivo*, although similar measurements taken from histologic tissue sections must account for shrinkage and deformation due to the chemical processing. The analysis of volumes over time can provide information about growth rates for individual metastases. Overall, MRI can provide a much more complete picture of brain metastasis than can traditional histology.

In this study, we assessed the metastatic potential of two highly brain metastatic human breast cancer cell lines (231-BR and 231-BR-HER2) by quantifying the number of metastases and their volumes over the entire brain of each mouse, at multiple time points. This study provides *in vivo* information about when and where metastases develop in these models of breast cancer metastasis to the brain. This is the first report of the *in vivo* spatial and temporal monitoring of the development of experimental metastasis in the whole mouse brain by MRI.

Materials and Methods

Cell Culture

Two human breast cancer cell lines were used: (i) MDA-MB-231BR (231-BR), which is a highly brain metastatic derivative of the human MDA-MB-231 breast cancer cell line [11]; and (ii) MDA-MB-231BR/HER2 (231-BR-HER2), a version of 231-BR that is transfected with the *HER2* gene [19]. Both cell lines were previously transfected with enhanced green fluorescent protein (EGFP) under the CMV promoter using a retroviral vector (pLEGFP-C1; BD Biosciences, Mississauga, Canada).

Cell lines were maintained in medium containing 10% fetal bovine serum at 37°C and 5% CO₂. Cells were labeled with a micrometer-sized superparamagnetic iron oxide particle as described previously [20]. Iron-labeled cells are visible in MR images as discrete regions of signal void. This allowed us to identify mice that received successful cell injections. All mice were scanned on the day of the injection and five of the eight mice per group, which showed obvious signal voids in the brain images, were included in the experiments. In one group of mice, the signal voids were used to assess the early distribution of the cancer cells in the brain after their arrest in the brain.

Animal Preparation

Nude mice (female, *nu/nu*, 6–8 weeks old, 18–22 g; Charles River Laboratories, Wilmington, MA) were anesthetized with isoflurane (2% in oxygen) and a 0.1-ml Hank's balanced salt solution containing the cancer cells was injected into the left ventricle of the beating

heart using a 27-gauge needle, as previously described [26]. Several experimental groups were compared.

Two groups of mice ($n = 5$ per group) were injected with 175,000 231-BR (mice 1–5) or 231-BR-HER2 (mice 6–10) cells and scanned on days 19, 23, 26, and 29 after injection. On the basis of a previous histologic analysis by Palmieri et al. [19], we expected that, at the end point, we would observe similar total numbers of metastases for the two cell lines but larger metastases in the brains of mice injected with the 231-BR-HER2 cells. This *in vivo* longitudinal imaging experiment was performed to expand on that histologic study by quantifying metastasis numbers, volumes, growth rates, and spatial distributions in the entire brain over time.

One group of mice ($n = 5$; mice 11–15) was injected with 50,000 231-BR-HER2 cells and scanned on day 29 after injection. Our hypothesis was that fewer metastases would form in the brains of mice injected with fewer cells and that the presence of fewer metastases in the brain would impact their size and distribution.

One additional group of five mice (mice 16–20) received 175,000 231-BR-HER2 cells and were scanned on days 1 and 35 after injection. This experiment was performed to compare the distribution of arrested cells, detected as discrete regions of signal void on day 1, with the distribution of brain metastases at the end point.

Magnetic Resonance Imaging

Imaging was performed on a 1.5-T GE CV/I clinical MR scanner (General Electric, Mississauga, Canada) using a custom-built gradient coil (maximum strength = 600 mT/m and peak slew rate = 2000 T/m per second). Before scanning, mice were anesthetized with isoflurane (2% in oxygen) and placed in a custom-built solenoidal mouse head radiofrequency (RF) coil (inner diameter = 1.5 cm). *In vivo* images were acquired using the three-dimensional balanced steady-state-free precession (bSSFP) pulse sequence with the following parameters: isotropic resolution = 200 μ m, repetition time = 5.4 milliseconds, echo time = 2.7 milliseconds, flip angle = 35°, signal averages = 4, receiver bandwidth = ± 31 kHz, RF phase cycles = 4, and scan time = 62 minutes. For the mice scanned on day 1, the repetition time/echo time was increased to 25/12.5 milliseconds to maximize the ability to detect signal voids due to iron [21,22] and the number of signal averages was reduced to 2 to keep the scan time under an hour. Other parameters remained the same. Scan time was 48 minutes. Zero filling was applied to all image data resulting in a displayed resolution of $33 \times 33 \times 100$ μ m after reconstruction.

Data Analysis

Brain metastases were counted manually in each set of images for all mice by a single observer (M.P.); each individual mouse scan resulted in 256 images. For the analysis of the distribution of metastases, the brain was divided into four regions: the olfactory, the cortex, the central brain, and the posterior brain. The olfactory region contained the olfactory bulb and the anterior olfactory nucleus. The cortex region contained the frontal cortex and the cerebral cortex. The central brain region included the hypothalamus, the thalamus, the midbrain, the caudate putamen, the ventral striatum, and the basal forebrain. The posterior brain consisted of the cerebellum, the pons, and the medulla. The number of metastases per region was presented as a percentage of the total number of metastases detected in the entire brain. This was determined for all brain regions at each time point for mice in each group.

Volumes (of the brain metastases, the whole brain, and the individual brain regions) were measured using the image analysis program VG Studio (Volume Graphics, Heidelberg, Germany). Statistical analyses were performed using GraphPad Prism software. Unpaired *t*-tests followed by Mann-Whitney *post hoc* tests were conducted to determine whether there were statistically significant differences between groups, time points, and brain regions ($P < .05$). Values are presented as mean \pm SE.

Results

Analysis of Whole Brain Image Data

Representative images of brain metastases (arrows) at each imaging time point are shown in Figure 1 for three brain locations in a

231-BR-HER2 mouse. The image contrast for bSSFP images is related to T_2/T_1 . Metastases appear with high signal intensity in the bSSFP images due to their high fluid content and longer T_2 compared with the brain parenchyma. Brain metastases were detected as early as 19 days after injection, the first imaging time point, for all mice (Table 1). The total number of metastases per whole brain at day 19 varied between 4 and 69 for 231-BR mice and between 17 and 64 for 231-BR-HER2 mice. At end point, there were between 49 and 165 metastases in 231-BR mice and between 34 and 202 metastases counted in the brains of 231-BR-HER2 mice. There was no significant difference in the mean number of metastases that developed in mice that were injected with 175,000 231-BR or 231-BR-HER2 cells at any imaging time point. The mean number of metastases at end point was 116 and 121, for 231-BR and 231-BR-HER2 mice, respectively.

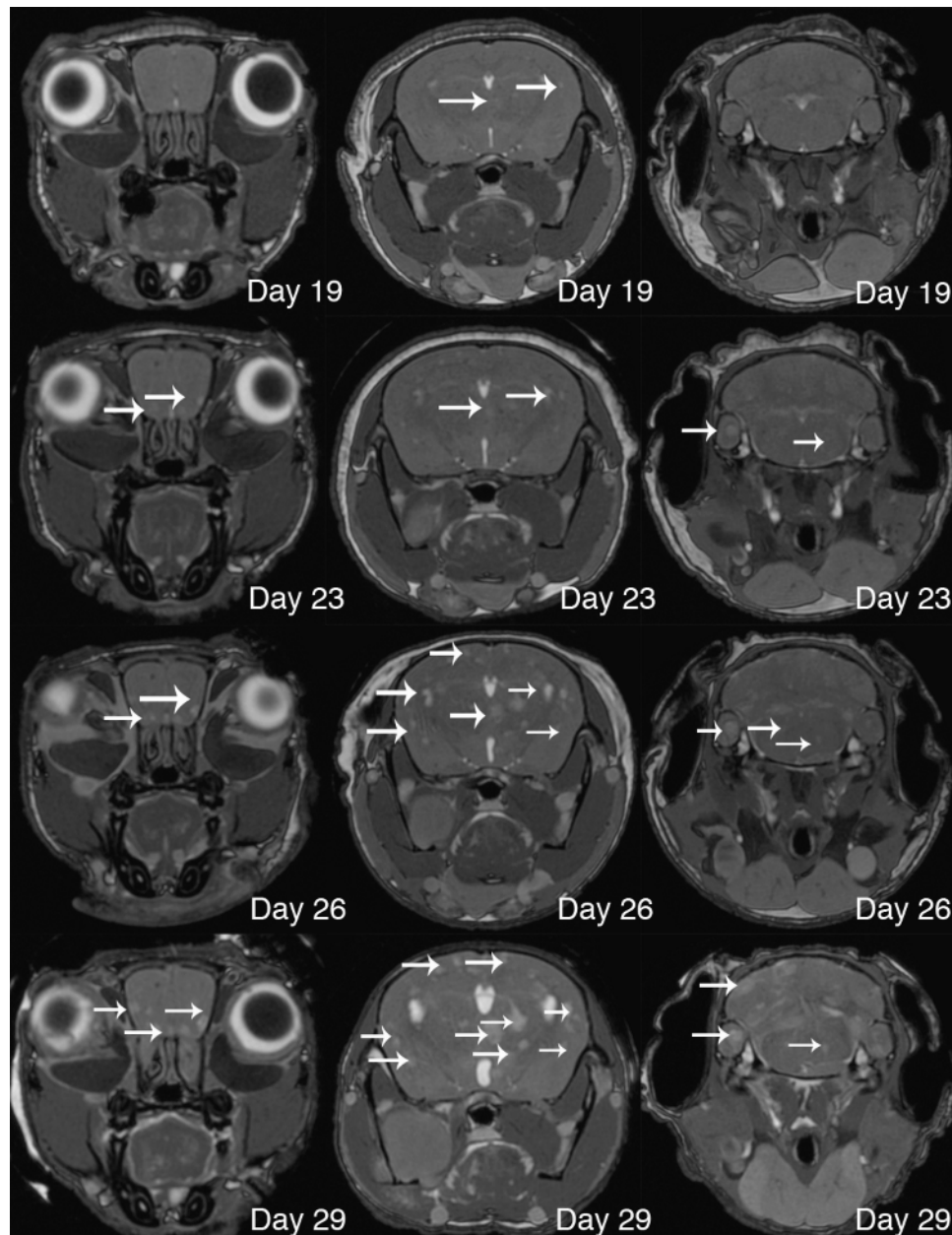


Figure 1. Monitoring tumor growth after injection of 231-BR-HER2 cells. Representative axial bSSFP mouse brain images showing the development of brain metastases for a mouse injected with 175,000 231-BR-HER2 cells. Each row shows three brain regions at a different time point for the same mouse. Metastases (white arrows) appear as regions with high signal intensity compared with normal brain.

Table 1. Summary of the Number of Metastases in Mice Injected with 231-BR or 231-BR-HER2 Cells.

Mouse	231-BR (175,000)				Mouse	231-BR-HER2 (175,000)				Mouse	231-BR-HER2 (50,000)	
	Day 19	Day 23	Day 26	Day 29		Day 19	Day 23	Day 26	Day 29		Day 29	
1	28	61	102	122	6	19	31	36	37	11	16	
2	33	48	114	—	7	55	134	—	—	12	27	
3	4	17	N/A	49	8	35	110	202	—	13	26	
4	20	64	84	130	9	64	135	191	197	14	13	
5	69	99	N/A	165	10	17	25	28	34	15	13	

Mice 1 to 5 received 175,000 231-BR cells, mice 6 to 10 received 175,000 231-BR-HER2 cells, and mice 11 to 15 received 50,000 231-BR-HER2 cells. The metastases were counted manually by assessing each image slice covering the whole mouse brain for sets of images obtained at each time point. A dash indicates that the mouse was killed before imaging could take place at that time point because of its health status. The numbers in boxes shaded gray indicate the number of metastases at the end point. The mean number of metastasis at end point was 116 for 175,000 231-BR, 121 for 175,000 231-BR-HER2, and 19 for 50,000 231-BR-HER2. N/A indicates not applicable.

The mean volume for all of the brain metastases in the five mice in each group was calculated for each time point, and this is shown in Figure 2. The mean volume was significantly larger for 231-BR-HER2 metastases at all time points. At day 19 after injection, the difference in the mean volumes is small but statistically significant, and by the last imaging session, the mean volume of the metastases in the 231-BR-HER2 mice was nearly twice that of the 231-BR mice (0.091 mm^3 for 231-BR and 0.165 mm^3 for 231-BR-HER2). Having longitudinal image data allowed us to calculate growth rates. The volume data were fit best by an exponential function with $R^2 = 0.98$ and $R^2 = 0.99$ for 231-BR-HER2 and 231-BR, respectively. The growth rate was 67.5% for 231-BR-HER2 metastases and 54.4% for 231-BR metastases.

Images from mice injected with two different numbers of 231-BR-HER2 cells showed that the mice injected with 50,000 cells developed far fewer metastases compared with mice that received 175,000 cells (Table 1). The mean number of metastases at end point was 19 and 121 for mice injected with 50,000 or 175,00 cells, respectively. The variability in the numbers of metastases was lower for mice that developed fewer metastases; the total number of metastases at day 29 for mice that received 50,000 cells varied between 13 and 27. The mean volume of metastases that developed in mice injected with 50,000 231-BR-HER2 cells was significantly larger than in mice

that received 175,000 231-BR-HER2 cells; 0.22 mm^3 compared with 0.17 mm^3 , respectively.

Spatial Distribution of Metastases

In mice injected with 175,000 231-BR-HER2 or 231-BR cells, most brain metastases were located in the cortex and central brain regions. Figure 3 shows the percentages of metastases located in each brain region, at each time point. At day 29, more than 90% of all brain metastases were located in the cortex and central brain regions for both 231-BR-HER2 and 231-BR mice. More precisely, in 231-BR-HER2 mice at day 29 (Figure 3A), $51.9\% \pm 3.5\%$ of metastases were in the cortex, $31.1\% \pm 4.1\%$ were in the central brain, $12.7\% \pm 4.4\%$ were in the posterior brain, and $4.28\% \pm 3.7\%$ of metastases were located in the olfactory region. In 231-BR mice at day 29 (Figure 3B), the distribution of metastases was $62\% \pm 5.1\%$, $30\% \pm 2.2\%$, $4.5\% \pm 2.3\%$, and $3.6\% \pm 2.6\%$ for the cortex, the central brain, the posterior brain, and the olfactory regions, respectively. Asterisks in Figure 3B indicate where there are significant differences between the two cell lines. Over time, the percentage of 231-BR-HER2 metastases in the cortex (Figure 3A, gray bars) decreased, as the percentage in the olfactory and posterior brain regions increased, causing a shift in the final distribution. The percentage of metastases in the cortex was significantly higher for the 231-BR line compared with the 231-BR-HER2 cell line,

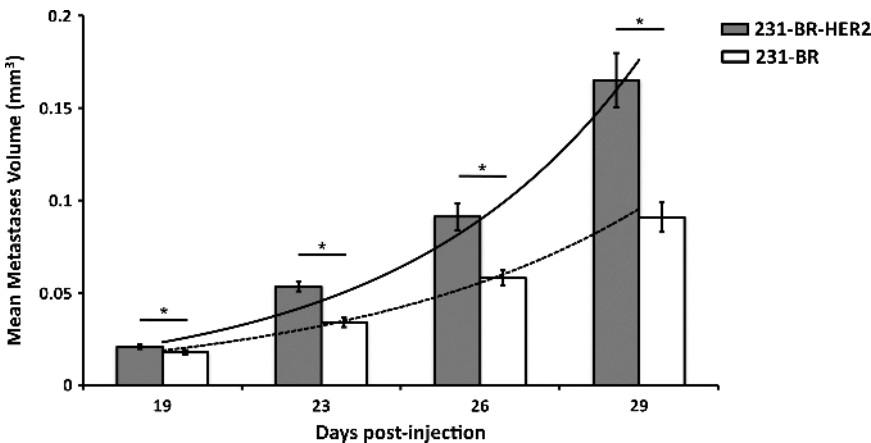


Figure 2. Mean metastases volumes in the whole brain for 231-BR-HER2 and 231-BR mice. At each time point, the mean metastasis volume was calculated for all metastases in all mice in each group. The mean volume was significantly greater for 231-BR-HER2 mice (gray bars) compared with 231-BR mice (white bars) at every time point ($*P < .05$). The mean volumes increased between each time point for both cell lines (significant at $P < .05$). An exponential growth curve fits the data best for each cell line. The growth rates were 67.5%, with $R^2 = 0.98$ for 231-BR-HER2 metastases (solid line) and 54.4% with $R^2 = 0.99$ for 231-BR metastases (dashed line).

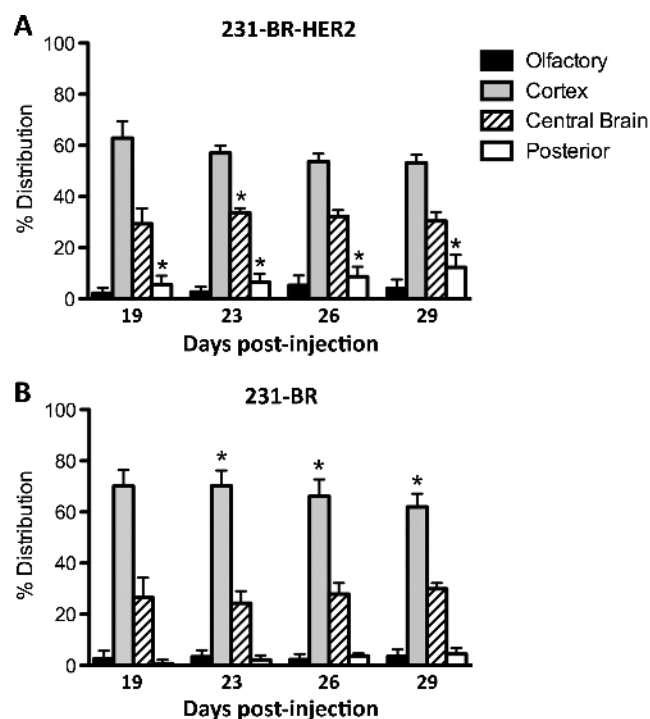


Figure 3. Relative distribution of metastases in the brain for 231-BR-HER2 and 231-BR mice. The percent distribution of tumors in each brain region is shown for all time points for 231-BR-HER2 mice (A) and 231-BR mice (B). The asterisks denote a statistically significance difference ($P < .05$) between the two cell lines.

at days 23, 26, and 29. The percentage of metastases in the posterior region was significantly higher for the 231-BR-HER2 cell line at all time points. The percentage of metastases in the central brain was significantly higher for the 231-BR-HER2 cell line at day 23.

To determine whether the number of brain metastases that developed in each brain region was merely related to the size of the predefined brain regions (i.e., there were more metastases just because the region is larger), the volumes of the four brain regions were calculated (Table 2). The individual brain region volumes were as follows: cortex = 141.5 mm^3 , central brain = 143.1 mm^3 , posterior brain = 104.8 mm^3 , and olfactory region = 22.4 mm^3 . The mean volume of the whole brain was 411.5 mm^3 . Therefore, the cortex occupied approximately 34% of the whole brain; the central brain, 35%; the posterior brain, 26%; and the olfactory region, 5% (Table 2). The mean volumes of the cortex and the central brain were nearly equal (141.5 and 143.1 mm^3 ,

respectively) despite large differences in the numbers of metastases. The mean percentage of metastases in the cortex and central brain at day 29 was significantly different for both cell lines; 62% versus 30% for 231-BR and 51.9% versus 31.1% for 231-BR-HER2. Despite very large differences in the mean volumes of the posterior and olfactory regions (104.8 and 22.4 mm^3 , respectively), there was no significant difference in the percentages of metastases in these regions at day 29 for either cell line. Furthermore, although the volume of the posterior brain region represents a quarter of the whole brain volume, only 12.7% and 4.5% of metastases from 231-BR-HER2 and 231-BR mice, respectively, were located in this region at day 29 (Figure 3 and Table 2). This analysis indicates that the size of the brain region is not the main determinant of the number of metastases developing within it.

Figure 4 shows the mean tumor volumes at each time point for each of the different brain regions. We compared the volumes of metastases in mice that received 175,000 231-BR (white bars) or 231-BR-HER2 (gray bars) cells. In the cortex, the mean tumor volume was significantly larger for 231-BR-HER2 mice compared with 231-BR mice at days 23, 26, and 29 after injection. In the central brain region, this was the case for all time points. The trend was similar for the posterior brain region, but no significant differences were measured for the olfactory regions.

We also looked to see whether the volumes of metastases were different in the various brain regions. There were notable differences at some time points. For example, at days 19 and 26, 231-BR-HER2 metastases were significantly larger in the central brain compared with those in the cortex and olfactory regions. At days 19 and 26, 231-BR metastases in the olfactory region were significantly larger than all other brain regions. Interestingly, by day 29, which is a typical end point for this sort of study, there were no differences detected in metastases volumes between the brain regions.

We were also able to assess growth rates for metastases within each brain region. The data for volume over time were reliably fit by an exponential trend line for all regions for 231-BR-HER2 metastases, except the olfactory region. In the olfactory region, a linear function best fit the data; the growth rate (27%) was also much lower than that of metastases in the other brain regions. Similarly, growth of the 231-BR metastases was exponential, except for that in the posterior region where neither linear nor exponential fits resulted in a sufficiently high R^2 value.

Comparing Voids Detected on Day 1 with Metastases Detected on Day 35

We imaged one group of mice injected with 175,000 231-BR-HER2 cells on days 1 and 35 to compare the distribution of the signal

Table 2. Summary of the Percentages of Metastases per Brain Region at Day 29 and the Corresponding Growth Rates for 231-BR and 231-BR-HER2 Mice.

Brain Regions	Volume (mm^3)	% Whole Brain	% Metastases at Day 29		Growth Rates (%)	
			231-BR	231-BR-HER2	231-BR	231-BR-HER2
Cortex	141.5 ± 9.1	34	$62.0 \pm 5.1^{*†}$	$51.9 \pm 3.5^†$	50 (exp, $R^2 = 0.95$)	65 (exp, $R^2 = 0.97$)
Central brain	143.1 ± 6.8	35	30.0 ± 2.2	31.1 ± 4.1	50 (exp, $R^2 = 0.96$)	67 (exp, $R^2 = 0.99$)
Posterior	104.8 ± 4.1	26	$4.5 \pm 2.3^*$	12.7 ± 4.4	N/A	72 (exp, $R^2 = 0.98$)
Olfactory	22.4 ± 3.4	5	3.6 ± 2.6	4.28 ± 3.7	65 (exp, $R^2 = 0.98$)	27 (line, $R^2 = 0.97$)

The volumes of the four brain regions (cortex, central, posterior, and olfactory) were measured and the percentage of the whole brain that they occupy was calculated. The percentages of metastases in each of these brain regions were determined for each cell line.

The best fit for the growth curves, the growth rates, and the R^2 were measured from the data in Figure 4. The R^2 value indicates the goodness of the fit (with $R^2 = 1$ meaning a perfect fit), exp = indicates an exponential growth, line = linear growth.

*Significant difference between the two cell lines ($P < .05$).

[†]Significant difference between the cortex and central brain regions ($P < .05$).

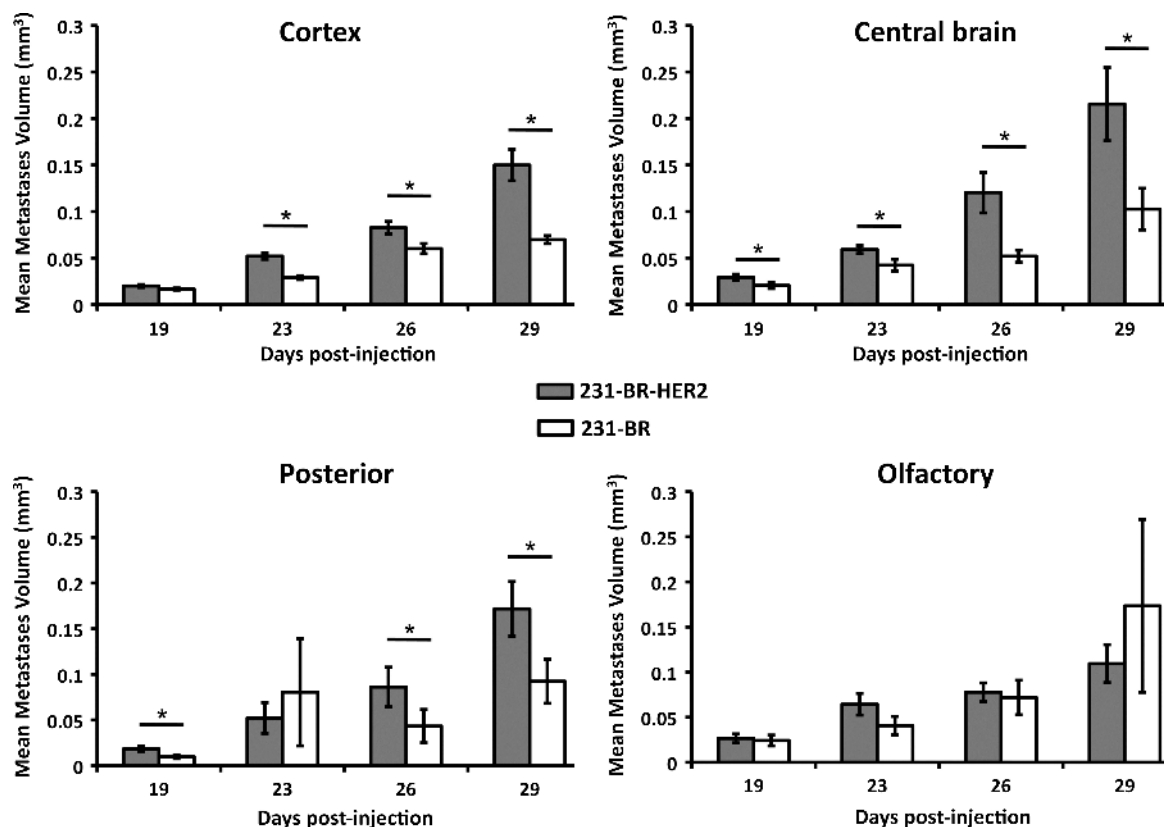


Figure 4. Mean metastases volumes in each brain region for 231-BR-HER2 and 231-BR mice. Mean volumes for metastases due to 231-BR-HER2 (gray bars) and 231-BR (white bars) cells in the cortex, central brain, posterior brain, and the olfactory brain region for each imaging time point. *Statistical significance ($P < .05$) between the two cell lines.

voids visible on day 1, due to the arrest of iron-labeled cells, with the distribution of brain metastases at end point (Figure 5). On day 1, approximately 50% of the void volume was located in the cortex, 28% in the central brain, 17% in the posterior brain, and 5% in the olfactory region (Figure 5B). On day 35, approximately 50% of the metastases were located in the cortex, 40% in the central brain, 8% in the posterior brain, and 2% in the olfactory region (Figure 5C).

The ratio of the “number of tumors at end point/void volume on day 1” was 1 for the cortex, 1.45 for the central brain region, and 0.45 and 0.24 for the posterior and olfactory brain regions, respectively. This suggests that a smaller proportion of the cells that arrest in the brain for the posterior and olfactory regions go on to form metastases compared with the cells that arrest in the cortex and central brain regions and that both the initial arrest and the survival of cells in particular brain regions is important.

Discussion

In the current work, we demonstrate how MRI can be used to study cancer progression with high spatial resolution, excellent soft tissue contrast, and with the ability to image an entire organ longitudinally over time. We used MRI to compare brain metastases due to two different human breast cancer cell lines; 231-BR, which is a brain metastatic derivative of the parental MDA-MB-231 cell line, established by Yoneda et al. [11], and 231-BR-HER2, a version of this cell line that was transfected with *HER2* by Palmieri et al. [19]. Many studies indicate that *HER2* overexpression correlates with more aggressive disease [23], increased metastatic potential [24], and a poorer prognosis [25] in patients with breast cancer. We also compared

metastases resulting from the injection of two different cell numbers for 231-BR-HER2.

The three-dimensional, high-resolution nature of MRI allowed us to quantify the total numbers of metastases in the whole brain for each mouse at every imaging time point. A large amount of data can be collected from relatively small numbers of animals this way; we counted 1184 metastases in the end point images of mice 1 to 10 alone. We found that there were similar numbers of metastases observed in the brain images for both 231-BR and 231-BR-HER2 cell lines; however, 231-BR-HER2 metastases developed significantly larger volumes than 231-BR metastases.

Palmieri et al. [19], who originally created the 231-BR-HER2 cell line, and who previously compared brain metastases due to 231-BR and 231-BR-HER2 through a histologic analysis, reported similar findings. The advantages of using MRI are that we were able to interrogate the whole brain at more than a single time point and to calculate the volumes of the MRI detectable brain metastases. By comparison, Palmieri et al. assessed one hemisphere of the brain at end point and used a grid to rank metastases visible in hematoxylin and eosin-stained sections as either large ($>50 \mu\text{m}^2$) or small ($<50 \mu\text{m}^2$). MRI provided additional information that was not possible to glean from a conventional histologic study. The longitudinal data showed that new metastases appeared at each imaging time point, for both cell lines, up to and including the end point scans. Longitudinal MRI also allowed us to look at growth rates and showed that growth rate for 231-BR-HER2 metastases was greater than that for 231-BR. Importantly, MRI revealed that metastases due to the 231-BR-HER2 cell line were significantly larger than those from 231-BR from the earliest time point

they were detectable by MRI (day 19). These data provide additional evidence that HER2 overexpression has a pronounced effect on breast cancer metastatic growth in the brain and suggest that whatever mediates HER2 aggressiveness happens early.

Another interesting finding was our observation that, for both 231-BR and 231-BR-HER2 cell lines, animals that developed fewer brain metastases had larger metastases. This may be related to the fact that there is more room within the intracranial space for a smaller number of metastases to grow [26]. Likewise, growth may be limited, when there are large numbers of metastases, by competition for resources. Kuang et al. [27] used detailed mathematical modeling to demonstrate the potential growth limitations that a tumor may experience when competing for resources with the surrounding healthy tissue. Our observation of larger metastases in the brains of mice with fewer metastases is a novel finding that was possible because of our whole brain imaging approach.

The main limitation of MRI when compared with histology is spatial resolution. The smallest metastasis detected with MRI in this study was 0.001 mm^3 (this represent a three-dimensional image voxel of $100 \times 100 \times 100 \text{ }\mu\text{m}$). Still, most histologic studies that have looked at brain metastases in stained sections consider a micrometastasis to be on the order of $50 \text{ }\mu\text{m}$ in diameter or less [19]. A single micrometastasis may therefore go undetected or, a closely spaced collection of multiple micrometastases may appear as a single metastasis, using our MRI protocols. Furthermore, the MRI described in this study does not provide any molecular information, whereas immunohistochemistry can. However, one of the main advantages of MRI is its noninvasive nature, which allows for multiple time point analyses on live animals. Thus, MRI and microscopy are complementary and together can provide information at the small animal, cellular, and molecular levels.

Three-dimensional MRI also allowed us to examine the full spatial distribution of metastases in the brain. Overall, we found that a larger

percentage of the metastases were located in the cortex and central brain regions, with smaller numbers of metastases in the olfactory and posterior brain regions, for both cell lines. Our findings are similar to those of Fitzgerald et al. [28] who reported a nonrandom distribution of brain metastases for 231-BR cells in nude mice. They identified the locations of metastases for each mouse in a binary fashion, by indicating that they were, or were not, present in stained sections from a number of brain locations at end point. In contrast, three-dimensional MRI permitted a comprehensive and quantitative assessment of the percentages of metastases in each of the different brain regions, and changes in these patterns with time. MRI revealed that, for the 231-BR cell line, the distribution of brain metastases remained fairly uniform over time. However, for the 231-BR-HER2 cell line, the proportion of metastases located in the posterior brain region increased with time, reducing the percentage of the cortex occupied by metastases, with the result that, at days 23, 26, and 29 after injection, the number of metastases that were detected in the cortex was greater for the 231-BR cell line. This type of analysis within the same mouse is not possible by histology.

To the best of our knowledge, this study is the first to provide quantitative imaging data on the temporal and spatial development of brain metastases in the mouse. Ribot et al. [22] have previously used the 231-BR brain metastasis model in nude mice to develop the bSSFP imaging sequence for the detection of both metastasis and iron-labeled cells. The blood-brain permeability associated with developing 231-BR brain metastases was studied by Percy et al. [29]. Song et al. [30] have established a nude rat model of breast cancer brain metastasis using the 231-BR cell line, transfected with the luciferase gene, and evaluated it using MRI (of the brain) and bioluminescence imaging (BLI). The percentages of animals with metastases in the brain, the spinal cord, the visceral organs, or the bone were determined through the analysis of MRI, BLI, and histology. Unexpected skeletal metastases in the spine were reported for the first time, pointing to the

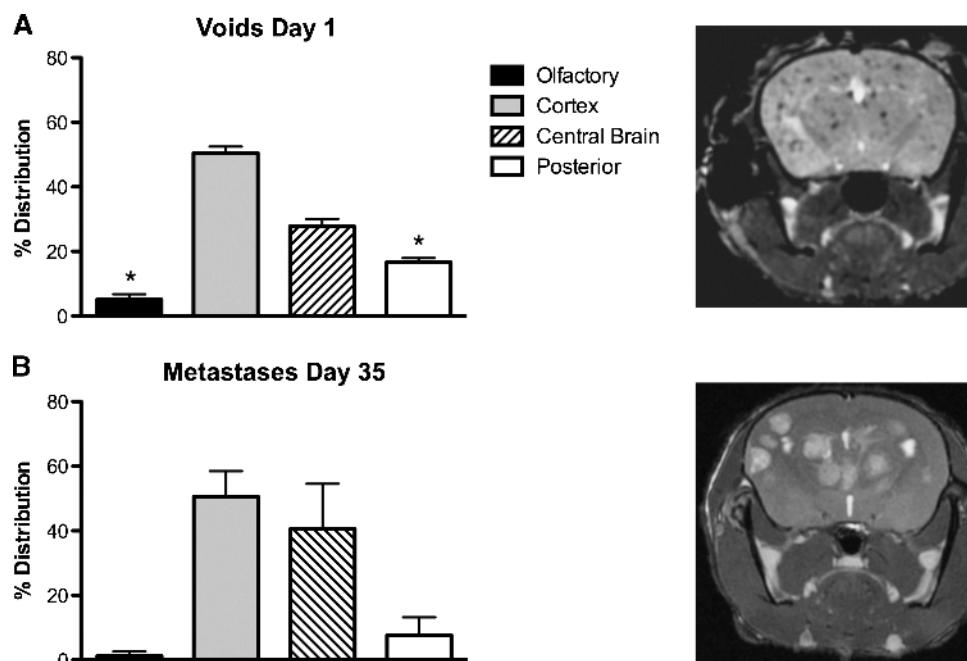


Figure 5. Distribution of signal voids on day 1 after injection (A) and of metastases at day 35 (B) for a group of 231-BR-HER2 mice. The void volume and the number of metastases were measured for each brain region. *Statistical significance ($P < .05$) between the void and the metastasis distribution.

value of whole body and multimodality imaging. Brain metastases, detected by MRI and histology, were not visible by BLI, indicating that this imaging modality is not optimal for brain studies.

Palmieri et al. [19] used fluorescence imaging to detect the EGFP associated with the 231-BR-HER2 cell line in excised mouse brains. Although they reported a general trend of increasing fluorescent metastases with greater HER2 overexpression, quantification of these images was not possible because of low resolution, autofluorescence, and overlap of the fluorescent signal from nearby metastases.

By prelabeling cancer cells with iron oxide nanoparticles, we could visualize the distribution of these cells throughout the whole, intact brain soon after their arrest. Previous work in our laboratory has validated that the discrete regions of signal void, detected by MRI at day 1, represent individual iron-labeled cells or small clusters of cells trapped in brain capillaries [31]. We quantified the volume of signal loss in each brain region on day 1 and compared this with the distribution of metastases in these brain regions at day 35. This experiment provided unique information about cancer cells in the brain of the same animals, at two time points after their injection, which is not possible with any other method. This analysis revealed that, in the cortex, the number of metastases that develop was directly related to the number of cells arresting there. This was similar for the central brain region, although not as linear. However, in the brain regions where far fewer metastases developed, the olfactory and posterior regions, the trend was reversed. This suggests that the microenvironment in the posterior and olfactory regions does not support the growth of brain metastases as well as the cortex and central brain regions. Previous studies have shown that the initial arrest of cancer cells in the brain is related to blood flow [28] and the presence of gray matter/white matter junctions [32]. Our results support these notions because the cortex contains the most blood vessels and the highest number of gray matter/white matter junctions when compared with the other brain regions we examined [32].

In this study, bSSFP images were acquired on a clinical system along with a custom-built high-performance gradient insert, which allowed for the higher resolution needed for mouse imaging. The bSSFP sequence is widely available on clinical scanners and gradient coils on modern clinical scanners can reach 50 mT/m, which is approximately the gradient strength we used in these studies. To date, bSSFP has been used mainly for cardiac imaging [33,34]. However, bSSFP is finding more use clinically for improving brain lesion detection and treatment. Pastel et al. [35] demonstrated that, because of its high spatial resolution, bSSFP was able to help differentiate small pineal cysts from tumors. Xie et al. [36] have noted the potential of bSSFP to help delineate fine brain structures in endonasal surgical treatment of tumors, once again because of its high resolution. In the future, the application of this technique on humans could lead to new information about breast cancer metastases to the brain, leading to adapted therapy strategies.

Conclusions

MRI is a powerful method for investigating preclinical models of cancer and metastasis. We have shown that longitudinal imaging of developing brain metastases can provide abundant data on the numbers and sizes of metastases as well as the rate of growth of brain metastases. This technology will provide new information about metastasis in the brain by allowing individual metastases to be scrutinized as they develop over time or as they change in response to treatment.

Acknowledgments

The authors thank Drs Brian Rutt, Andrew Alejski, and Francisco Martinez for their assistance with MRI hardware design, construction, and maintenance.

References

- [1] Lockman PR, Mittapalli RK, Taskar KS, Rudraraju V, Gril B, Bohn KA, Adkins CE, Roberts A, Thorsheim HR, Gaasch JA, et al. (2010). Heterogeneous blood-tumor barrier permeability determines drug efficacy in experimental brain metastases of breast cancer. *Clin Cancer Res* **16**, 5664–5678.
- [2] Weil RJ, Palmieri DC, Bronder JL, Stark AM, and Steeg PS (2005). Breast cancer metastasis to the central nervous system. *Am J Pathol* **167**, 913–920.
- [3] Lin NU, Bellon JR, and Winer EP (2004). CNS metastases in breast cancer. *J Clin Oncol* **22**, 3608–3617.
- [4] DiStefano A, Yong Yap Y, Hortobagyi GN, and Blumenschein GR (1979). The natural history of breast cancer patients with brain metastases. *Cancer* **44**, 1913–1918.
- [5] Kamar FG and Posner JB (2010). Brain metastases. *Semin Neurol* **30**, 217–235.
- [6] Bendell JC, Domchek SM, Burstein HJ, Harris L, Younger J, Kuter I, Bunnell C, Rue M, Gelman R, and Winer E (2003). Central nervous system metastases in women who receive trastuzumab-based therapy for metastatic breast carcinoma. *Cancer* **97**, 2972–2977.
- [7] Pestalozzi BC, Zahrieh D, Price KN, Holmberg SB, Lindtner J, Collins J, Crivellari D, Fey MF, Murray E, Pagani O, et al. (2006). Identifying breast cancer patients at risk for central nervous system (CNS) metastases in trials of the International Breast Cancer Study Group (IBCSG). *Ann Oncol* **17**, 935–944.
- [8] Church DN, Modgil R, Gugliani S, Bahl A, Hopkins K, Braybrooke JP, Blair P, and Price CGA (2008). Extended survival in women with brain metastases from HER2 overexpressing breast cancer. *Am J Clin Oncol* **31**, 250–254.
- [9] Stemmler HJ, Kahler S, Siekiera W, Untch M, Heinrich B, and Heinemann V (2006). Characteristics of patients with brain metastases receiving trastuzumab for HER2 overexpressing metastatic breast cancer. *Breast* **15**, 219–225.
- [10] Baculi RH, Suki S, Nisbett J, Leeds N, and Groves M (2001). Meningeal carcinomatosis from breast carcinoma responsive to trastuzumab. *J Clin Oncol* **19**, 3297–3298.
- [11] Yoneda T, Williams PJ, Hiraga T, Niewolna M, and Nishimura R (2001). A bone-seeking clone exhibits different biological properties from the MDA-MB-231 parental human breast cancer cells and a brain-seeking clone *in vivo* and *in vitro*. *J Bone Miner Res* **16**, 1486–1495.
- [12] Chen EI, Hewel J, Krueger JS, Tiraby C, Weber MR, Kralli A, Becker K, Yates JR, and Felding-Habermann B (2007). Adaptation of energy metabolism in breast cancer brain metastases. *Cancer Res* **67**, 1472–1486.
- [13] Kim LS, Huang S, Lu W, Chelouche Lev D, and Price JE (2004). Vascular endothelial growth factor expression promotes the growth of breast cancer brain metastases in nude mice. *Clin Exp Metastasis* **21**, 107–118.
- [14] Palmieri D, Lockman PR, Thomas FC, Hua E, Herring J, Hargrave E, Johnson M, Flores N, Qian Y, Vega-Valle E, et al. (2009). Vorinostat inhibits brain metastatic colonization in a model of triple-negative breast cancer and induces DNA double-strand breaks. *Clin Cancer Res* **15**, 6148–6157.
- [15] Tsai MS, Shamon-Taylor LA, Mehmi I, Tang CK, and Lupu R (2003). Blockage of heregulin expression inhibits tumorigenicity and metastasis of breast cancer. *Oncogene* **22**, 761–768.
- [16] Yano S, Shinohara H, Herbst RS, Kuniyasu H, Bucana CD, Ellis LM, Davis DW, McConkey DJ, and Fidler IJ (2000). Expression of vascular endothelial growth factor is necessary but not sufficient for production and growth of brain metastasis. *Cancer Res* **60**, 4959–4967.
- [17] Thomas FC, Taskar K, Rudraraju V, Goda S, Thorsheim HR, Gaasch JA, Mittapalli RK, Palmieri D, Steeg PS, Lockman PR, et al. (2009). Uptake of ANG1005, a novel paclitaxel derivative, through the blood-brain barrier into brain and experimental brain metastases of breast cancer. *Pharm Res* **26**, 2486–2494.
- [18] Lunt SJ, Cawthorne C, Ali M, Telfer BA, Babur M, Smigova A, Julian PJ, Price PM, Stratford IJ, Bloomer WD, et al. (2010). The hypoxia-selective cytotoxin NLCQ-1 (NSC 709257) controls metastatic disease when used as an adjuvant to radiotherapy. *Br J Cancer* **103**, 201–208.
- [19] Palmieri D, Bronder JL, Herring JM, Yoneda T, Weil RJ, Stark AM, Kurek R, Vega-Valle E, Feigenbaum L, Halverson D, et al. (2007). Her-2 overexpression increases the metastatic outgrowth of breast cancer cells in the brain. *Cancer Res* **67**, 4190–4198.

- [20] Heyn C, Ronald JA, Ramadan SS, Snir JA, Barry AM, MacKenzie LT, Mikulis DJ, Palmieri D, Bronder JL, Steeg PS, et al. (2006). *In vivo* MRI of cancer cell fate at the single cell level in a mouse model of breast cancer metastasis to the brain. *Magn Reson Med* **56**, 1001–1010.
- [21] Bernas LM, Foster PJ, and Rutt BK (2010). Imaging iron loaded mouse glioma tumors with bSSFP at 3T. *Magn Reson Med* **64**, 23–31.
- [22] Ribot EJ, Martinez-Santesteban FM, Simedrea C, Steeg PS, Chambers AF, Rutt BK, and Foster PJ (2011). *In vivo* single scan detection of both iron-labeled cells and breast cancer metastases in the mouse brain using balanced steady-state free precession imaging at 1.5 T. *J Magn Res Imaging* **34**, 231–238.
- [23] Camp RL, Dolled-Filhart M, King BL, and Rimm DL (2003). Quantitative analysis of breast cancer tissue microarrays shows that both high and normal levels of HER2 expression are associated with poor outcome. *Cancer Res* **63**, 1445–1448.
- [24] Hicks DG, Short SM, Prescott NL, Tarr SM, Coleman KA, Yoder BJ, Crowe JP, Choueiri TK, Dawson AE, Budd GT, et al. (2006). Breast cancers with brain metastases are more likely to be estrogen receptor negative, express the basal cytokeratin CK5/6, and overexpress HER2 or EGFR. *Am J Surg Pathol* **30**, 1097–1104.
- [25] Tandon AK, Clark GM, Chamness GC, Ullrich A, and McGuire WL (1989). HER-2/neu oncogene protein and prognosis in breast cancer. *J Clin Oncol* **7**, 1120–1128.
- [26] Andrews PJD and Citerio G (2004). Intracranial pressure. Part one: historical overview and basic concepts. *Intensive Care Med* **30**, 1730–1733.
- [27] Kuang Y, Nagy JD, and Elser JJ (2004). Biological stoichiometry of tumor dynamics: mathematical models and analysis. *Disc Cont Dyn Syst Ser B* **4**, 221–240.
- [28] Fitzgerald DP, Palmieri D, Hua E, Hargrave E, Herring JM, Qian Y, Vega-Valle E, Weil RJ, Stark AM, Vortmeyer AO, et al. (2008). Reactive glia are recruited by highly proliferative brain metastases of breast cancer and promote tumor cell colonization. *Clin Exp Metastasis* **25**, 799–810.
- [29] Percy DB, Ribot EJ, Chen Y, McFadden C, Simedrea C, Steeg PS, Chambers AF, and Foster PJ (2011). *In vivo* characterization of changing blood-tumor barrier permeability in a mouse model of breast cancer metastasis. A complementary magnetic resonance imaging approach. *Invest Radiol* **46**, 718–725.
- [30] Song HT, Jordan EK, Lewis BK, Liu W, Ganjei J, Klaunberg B, Despres D, Palmieri D, and Frank JA (2009). Rat model of metastatic breast cancer monitored by MRI at 3 tesla and bioluminescence imaging with histological correlation. *J Transl Med* **7**, 88.
- [31] Heyn C, Ronald JA, Mackenzie LT, MacDonald IC, Chambers AF, Rutt BK, and Foster PJ (2006). *In vivo* magnetic resonance imaging of single cells in mouse brain with optical validation. *Magn Reson Med* **55**, 23–29.
- [32] Hwang TL, Close TP, Grego JM, Brannon WL, and Gonzales F (1996). Prediction of brain metastasis in gray and white matter junction and vascular border zones. *Cancer* **77**, 1551–1555.
- [33] Uribe S, Beerbaum P, Sangild TS, Rasmusson A, Razavi R, and Schaeffter T (2009). Four-dimensional (4D) flow of the whole heart and great vessels using real-time respiratory self-gating. *Magn Reson Med* **62**, 984–992.
- [34] Sung K, Lee HL, Hu HH, and Nayak KS (2010). Prediction of myocardial signal during CINE balanced SSFP imaging. *Magn Reson Mater Phy* **23**, 85–91.
- [35] Pastel DA, Mamourian AC, and Duhaime AC (2009). Internal structure in pineal cysts on high-resolution magnetic resonance imaging: not a sign of malignancy. *J Neurosurg Pediatr* **4**, 81–84.
- [36] Xie T, Zhang XB, Yun H, Hu F, Yu Y, and Gu Y (2011). 3D-FIESTA MR images are useful in the evaluation of the endoscopic expanded endonasal approach for midline skull-base lesions. *Acta Neurochir* **153**, 12–18.